Nanoscale Res Lett (2010) 5:1982–1991
DOI 10.1007/s11671-010-9736-5

NANO EXPRESS

Surface Modification and Planar Defects of Calcium Carbonates by Magnetic Water Treatment

C. Z. Liu · C. H. Lin · M. S. Yeh · Y. M. Chao · P. Shen

Received: 7 June 2010 / Accepted: 5 August 2010 / Published online: 18 August 2010

Abstract Powdery calcium carbonates, predominantly calcite and aragonite, with planar defects and cation–anion mixed surfaces as deposited on low-carbon steel by magnetic water treatment (MWT) were characterized by X-ray diffraction, electron microscopy, and vibration spectroscopy. Calcite were found to form faceted nanoparticles having 3x $(0\bar{1}14)$ commensurate superstructure and with well-developed $\{11\bar{2}0\}$ and $\{10\bar{1}4\}$ surfaces to exhibit preferred orientations. Aragonite occurred as laths having 3x $(0\bar{1}1)$ commensurate superstructure and with well-developed $(0\bar{1}1)$ surface extending along [100] direction up to micrometers in length. The (hkil)-specific coalescence of calcite and rapid lath growth of aragonite under the combined effects of Lorentz force and a precondensation event account for a beneficial larger particulate/colony size for the removal of the carbonate scale from the steel substrate. The coexisting magnetite particles have well-developed {011} surfaces regardless of MWT.

Keywords Calcium carbonate · Nanoparticle · Magnetic water treatment · Surface modification · Superstructure · TEM

Introduction

Since the first patent registration by Vermeiren [1], magnetic water treatment (MWT) plays an increasingly important industrial role regarding scale control and amelioration of dispersion separations in hard water with troublesome deposition of calcium carbonate/sulfate and/or silica. The parameters that affect the MWT efficiency such as temperature, pH, strength and direction of the applied field, and the impurity elements present in hard water have been studied [2–8].

The underlying mechanism of MWT is complex involving the modified crystallization of scale-forming components and modified dispersion stability. These effects cannot be explained by magnetic attraction among the dispersed particles of iron oxides [9, 10], because the main scale component form fine nonmagnetic particles, such as calcium carbonate, gypsum and silica. Instead, an explanation was found in the changes of pH [11] or ion distribution/hydration near the dispersed particles to form neutralized surfaces for magnetically enhanced coagulation [12–14]. Theoretically, surface modification of the dispersed particles under magnetohydrodynamic forces, mainly Lorentz force, was affected by the conductivity of the solution, the flow velocity of the fluid, the retention time of dispersion in the working channel, and the flux density of the field [14]. However, the specific surfaces of a crystalline particle that tend to be neutralized by MWT were not studied.

For a calcium carbonate type scale, it has been established that a magnetic field caused preferential formation of a removable soft scale consisting of aragonite (orthorhombic, space group *Pmcn*) and minor vaterite (μ-$CaCO_3$, hexagonal, optically uniaxial positive), rather than a hard scale of calcite (trigonal, space group $R\bar{3}c$, optically uniaxial negative) [15, 16]. Transmission electron microscopy (TEM) has been used [16] to identify the calcium carbonate phases deposited from tap water and model water under the influence of a magnetic field. Aragonite and vaterite

C. Z. Liu · C. H. Lin · P. Shen (✉)
Department of Materials and Optoelectronic Science, National Sun Yat-sen University, Kaohsiung, Taiwan, R.O.C
e-mail: pshen@mail.nsysu.edu.tw

M. S. Yeh · Y. M. Chao
China Steel Incorporation, T64, Kaohsiung, Taiwan, R.O.C

nanocrystals were found to coexist in regularly shaped particle of micron size when crystallized in a magnetic field, whereas calcite crystals as large as submicron in size were suggested to be crystallized in the absence of a magnetic field [16]. However, the magnetically enhanced surface neutralization, and hence coagulation of $CaCO_3$ crystallites for a possible preferred orientation, was not reported.

In this work, size, shape, and defect microstructures of the powdery calcium carbonates deposited on the carbon steel by MWT were characterized in detail. We focused also on the (hkl)-specific surface neutralization, coalescence, and preferred orientation of the crystalline particles under the influence of a magnetic field, rather than the commonly adopted surface modification of colloidal particles by chemical stabilizers.

Experimental Section

Magnetic Water Treatment

The magnetohydrodynamic experiments were conducted in a circulation system ("Appendix 1") consisting of a tank filled with water pumping through a connected low-carbon steel pipe (0.25% C by weight), which was subjected to MWT under 100–400 G at the pipe center. The duration time of the direct magnetic influence was 0.1–0.2 s/cycle under a specified flow rate (0.5 m/s) of water originally filled with 400 ppm $CaCl_2$ and then added with 50 ppm $NaHCO_3$ per day. The pH varied from 7 to 8 at room temperature (20 ± 5°C) during MWT for a month forming a scale deposit typically 14 mg/cm^2 on a steel pipe or sheet. (A low-carbon steel sheet 0.2 cm in thickness was put in an arcrylic pipe connected to the carbon steel pipe for a comparative study of the scale deposit.) The steel pipe was optionally subjected to an electric ground to the Earth to see the possible change of phases and microstructures of the scale deposits.

Characterization

The crystalline phases of the powdery scale deposits were identified by X-ray diffraction (XRD, Cu Kα, 40 kV, 30 mA, using Siemens D5000 diffractometer), optical polarized microscopy, and scanning electron microscopy (SEM, JEOL JSM-6400, 20 kV) coupled with energy-dispersive X-ray (EDX) analysis. The scale powders collected on a silica glass substrate were mixed with KBr for Fourier transform infrared spectroscopy (FTIR, Bruker 66v/S. 64 scans with 4 cm^{-1} resolution) study. Raman spectrum of the scale powders was made using semiconductor laser excitation (532 nm, Jobin–Yvon Triax 320 Micro-Raman microprobe) having a resolution of 2 cm^{-1}.

The scale powders were collected on Cu grids overlain with a carbon-coated collodion film for TEM (FEI Tecnai G2 F20 at 200 kV and JEOL3010 at 300 kV) observations coupled with EDX analysis at a beam size of 10 nm. Bright-field image (BFI) and dark-field image (DFI) were used to study the size and shape of the crystalline phases. Selected area electron diffraction (SAED) pattern and lattice image coupled with two-dimensional Fourier transform and inverse transform were used to characterize surfaces, planar defects, and preferred orientation, if any, of the phases.

Results

The phase assemblages and microstructures of the scale deposit on low-carbon steel sheet and pipe are basically the same when subjected to MWT under an applied magnetic field of 100–400 G and duration of 0.1–0.2 s per cycle with or without an electric ground to the Earth, as indicated by the combined XRD, microscopic and vibrational spectroscopic results in the following.

XRD, Optical Microscopy and SEM

XRD of the powdery sample retrieved from the scale deposit on carbon steel subjected to MWT showed minor aragonite besides magnetite and the predominant calcite with strong {10$\bar{1}$4} and moderate {11$\bar{2}$0} diffractions due to (hkil)-specific preferred orientation (Fig. 1). Optical polarized micrographs under open and crossed polarizers (not shown) showed the birefringent calcite and aragonite particles were assembled/agglomerated up to a hundred

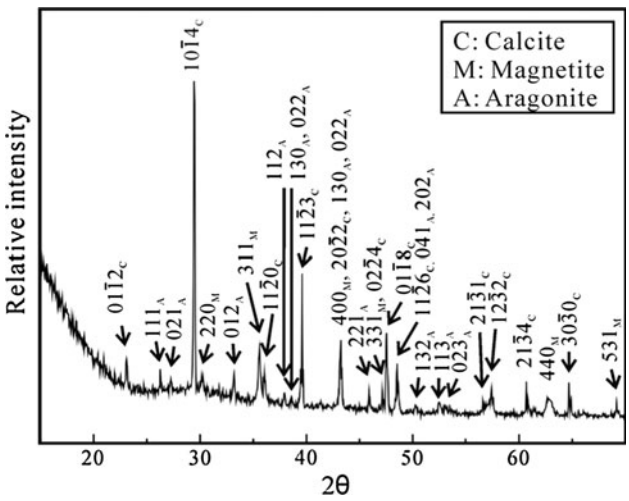

Fig. 1 XRD trace (CuKα) of the powdery sample retrieved from the deposit on the steel sheet subjected to MWT under 400 G at pipe center, 0.1 s/cycle and without an electric ground to the Earth

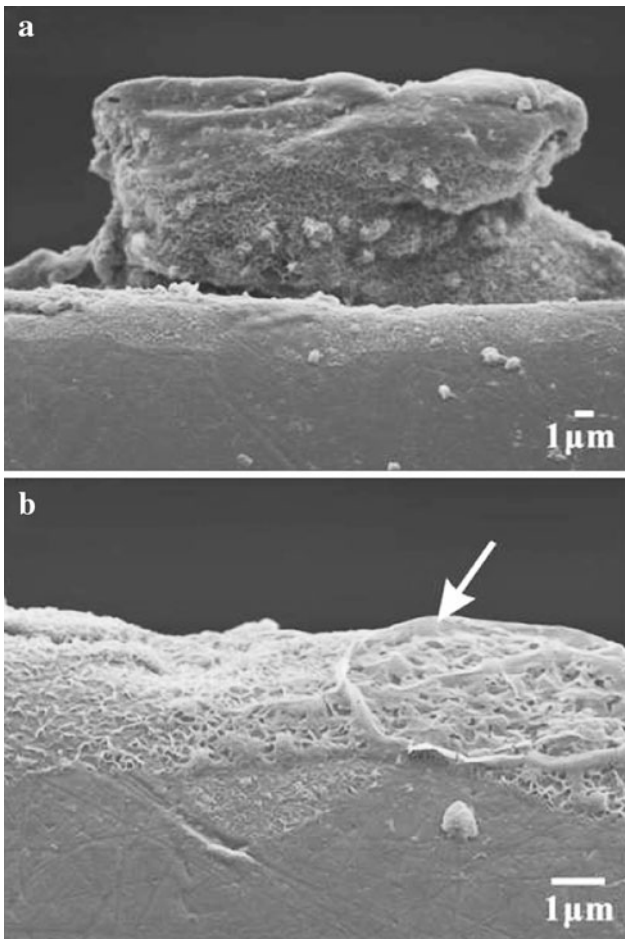

Fig. 2 SEM secondary electron image of a near cross-section view showing **a** broken scale ($CaCO_3$ + iron oxide) and **b** scale relic with mosaic pattern (*arrow*) on the steel substrate. The scale was formed by MWT under 400 G at pipe center, 0.2 s/cycle, and with an electric ground on the steel pipe and then cross-sectioned for this observation

microns in size, whereas opaque magnetite were assembled/agglomerated up to several hundred microns in size. SEM observations showed that the scale formed by MWT with an applied electric ground on the steel pipe were vulnerable to cross-sectioning (Fig. 2a). Still, mosaic scale relic on the pipe was recognized (Fig. 2b).

TEM

TEM BFI observation coupled with SAED pattern and EDX analyses of the powdery sample retrieved from the deposit on the steel pipe indicated that the magnetite and aragonite particles are much larger in size than the calcite nanoparticles. The submicron-sized magnetite particles were found to have well-developed $(0\bar{1}1)$ surface with minor {111} facets for the sample subject to MWT (Fig. 3) and that without an applied magnetic field (not shown) [17]. Occasionally, the magnetite particle formed twinned bicrystals with {111} twin plane and facets parallel to (100) besides {111} and much better developed {011} (Fig. 4).

The aragonite particle with negligible impurities typically occurred as laths having well-developed $(01\bar{1})$ surface extending along [100] direction up to micrometers in length (Fig. 5). There is additional 1/3 $(0\bar{2}2)$ diffraction in this case, implying the presence of a 3x commensurate superstructure parallel to the $(0\bar{1}1)$ plane.

The calcite nanoparticles with negligible Fe^{2+} and Fe^{3+} impurities, as indicated by the same EDX spectrum (not shown) as that of aragonite, were typically agglomerated in a close packed manner and tended to assemble by the $\{11\bar{2}0\}$ and $\{10\bar{1}4\}$ surfaces with preferred orientations to form elongate particulate up to microns in size (Fig. 6), which showed birefringence under optical polarized microscope (not shown). Lattice image (Fig. 7a) revealed further details of the individual calcite nanoparticles with well-developed $(1\bar{2}10)$ and $\{\bar{1}104\}$ surfaces both being edge on when viewed in $[40\bar{4}1]$ zone axis as indicated by 2-D forward and inverse Fourier transform in Fig. 7b and c, respectively. This accounts for $\{11\bar{2}0\}$- and $\{10\bar{1}4\}$-specific coalescence of such shaped calcite nanoparticles into particulates with $\{11\bar{2}0\}$ and $\{10\bar{1}4\}$ preferred orientations as manifested by XRD and SAED results. The calcite nanocrystal also showed 1-D commensurate superstructure with 3 times that of the $(0\bar{1}14)$ d-spacing (Fig. 7c). TEM observations of the scale formed without an applied magnetic field (not shown) indicated that the calcite and aragonite nanoparticles have poorly developed {hkil}-specific surfaces and are immune from commensurate superstructures [17].

Vibrational Spectroscopy

The FTIR analysis indicated a significant OH-signature ($\sim$3,400 cm^{-1}) for calcite, aragonite, and magnetite coexisting in the scale (Fig. 8a). The predominant calcite showed strong bands at 1,423 cm^{-1} for doubly degenerate asymmetric stretching, 875 cm^{-1} for out-of-plane bending, and 711 cm^{-1} for doubly degenerate planar bending based on previous assignments [18]. The shoulder on the low-frequency side of the 875 and 711 cm^{-1} band indicates a minor amount of aragonite that has characteristic doublet bands in such frequencies [18]. The broad band of magnetite at 595 cm^{-1} is significantly higher in wave number than that of natural minerals [19], possibly due to Fe^{3+}/Fe^{2+} ratio change and defects. The bands at 2,923 and 2,852 cm^{-1} are due to EtOH used for IR sample preparation.

The Raman shifts of coexisting calcite, aragonite and magnetite were shown in Fig. 8b. The aragonite showed bands with the assigned vibration modes in parenthesis at the following wave numbers: 145 (translational lattice mode), 269 (liberational lattice mode) 696, 704 doublets

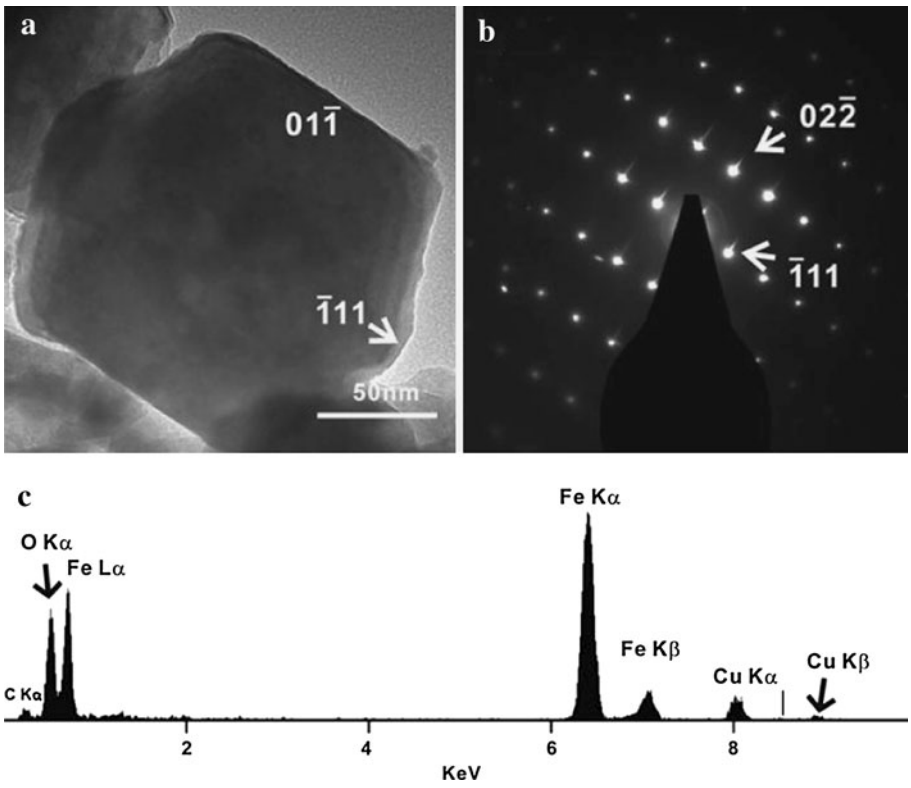

Fig. 3 TEM **a** BFI, **b** SAED pattern (Z = [211]) of a submicron-sized magnetite particle with well-developed (0$\bar{1}$1) face and {111} facets, **c** EDX spectrum indicating negligible impurities for the magnetite. The Cu counts were from the copper grids holding the specimen. The TEM sample was prepared from the same specimen as Fig. 1

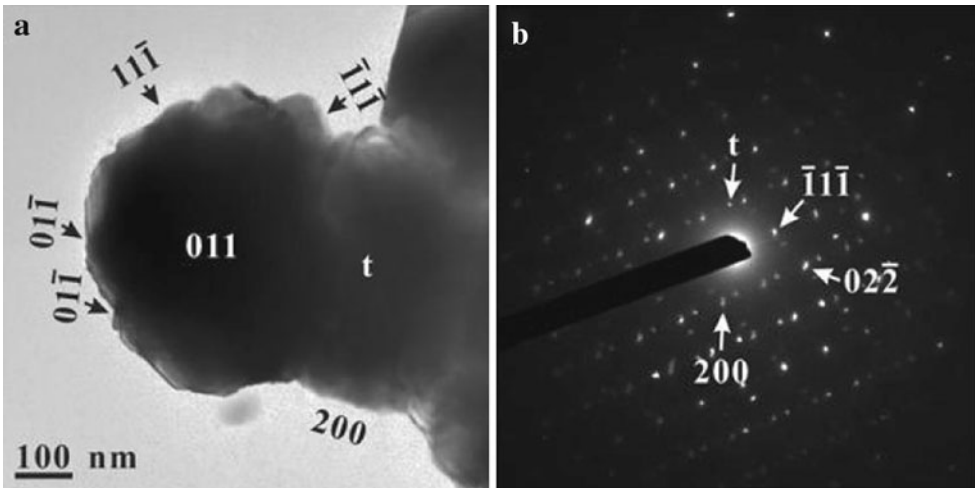

Fig. 4 TEM **a** BFI, **b** SAED pattern (Z = [011]) of submicron-sized and twinned magnetite bicrystals with well-developed (011) face in top view and {111} as well as (100) facets edge on. Scale sample on the steel pipe subjected to MWT under 400 G at pipe center, 0.2 s/cycle, and with an electric ground to the Earth

(B_{1g} and A_{1g}), and 1084 (v_1 symmetric stretching mode of CO_3^{2-}) according to the assignment of ref [20]. The bands at 145 (translational lattice mode), 269 (liberational lattice mode), 710 (v_4 in-plane bending mode of CO_3^{2-}), and 1084 (v_1 symmetric stretching mode of CO_3^{2-}) can be attributed to calcite following the assignment of ref [20]. The overtones of the 2 × v_2 mode at 1,740–1,750 cm^{-1} for calcite and aragonite [20] are obscured in the present Raman spectrum. The broad 217 (T_{2g}) and 449 (T_{2g}) bands of magnetite are slightly different from the reported wave numbers that are sensitive to the presence of defects and partial disorder [21]. In general, the vibrational bands of the individual phases vary slightly among the scale samples subjected to various MWT parameters (not shown) depending on the extent of lattice/polyhedra distortion.

Discussion

Nucleation and {hkil}-Coalescence Growth of Calcite with Preferred Orientation

The nucleation of calcite rater than vaterite in the present MWT can be attributed to the absence of biogenic

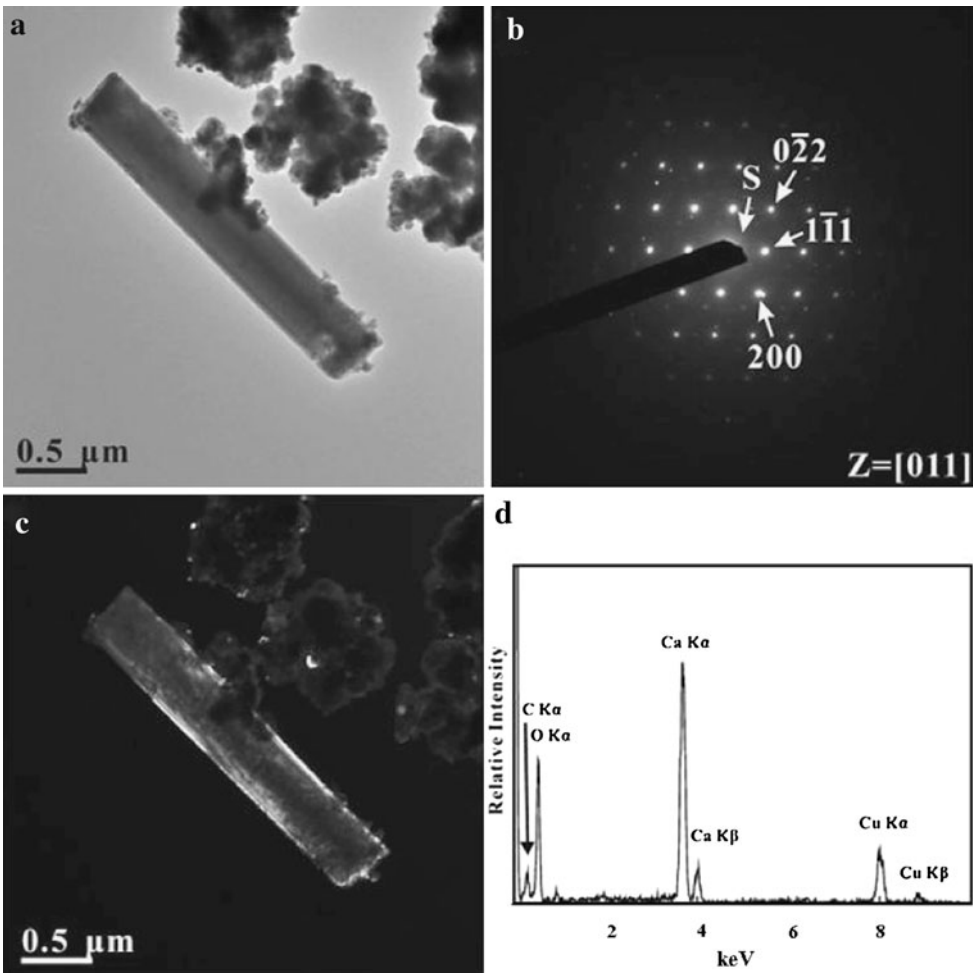

Fig. 5 TEM **a** BFI, **b** SAED pattern in [011] zone axis, **c** DFI using diffraction 02$\bar{2}$ and **d** EDX spectrum of an elongate aragonite particle with negligible impurities extending along [100] direction and with well-developed (0$\bar{1}$1) surface. The additional 1/3 (0$\bar{2}$2) diffraction (denoted as *S*) implies a 3x superstructure (cf. text). The scale sample was taken from the steel pipe subjected to MWT under 400 G at pipe center, 0.1 s/cycle, and with an electric ground to the Earth

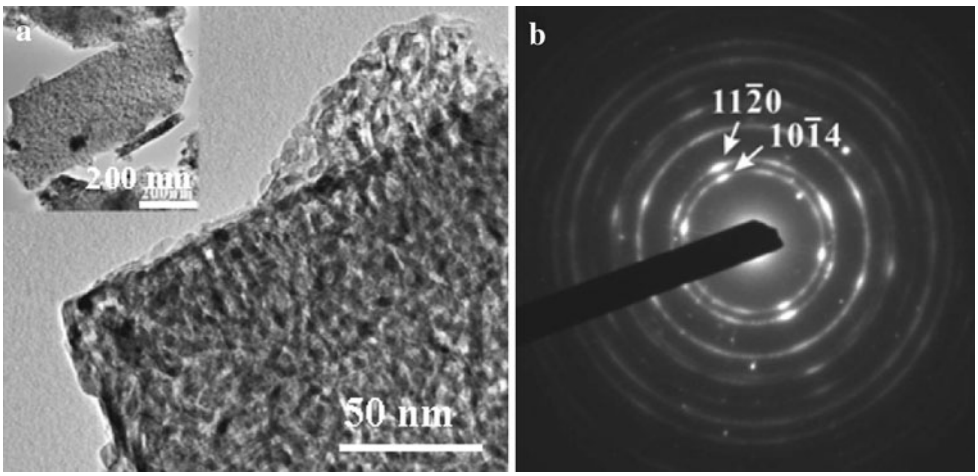

Fig. 6 TEM **a** BFI magnified from the figure inset, and **b** SAED pattern of randomly oriented calcite nanoparticles that were agglomerated up to microns in size with preferred orientations, as indicated by the {11$\bar{2}$0} and {10$\bar{1}$4} diffraction arcs. The TEM sample was prepared from the same specimen as Fig. 1

stabilizer and the presence of CO_2 gas in the dynamic flow condition, in view of CO_2 evaporation-induced kinetic formation of vaterite in a number of cryo-TEM experiments [22]). (Recent cryo-TEM study [22] indicated the template-controlled $CaCO_3$ formation starts with the formation of prenucleation clusters that aggregate leading to the nucleation of amorphous calcium carbonate nanoparticles in solution. These nanoparticles assemble at the template and, after reaching a critical size, develop dynamic crystalline domains (i.e. vaterite), one of which is selectively stabilized by the template.) The presence of Na^+ and Cl^- could also facilitate the formation of calcite

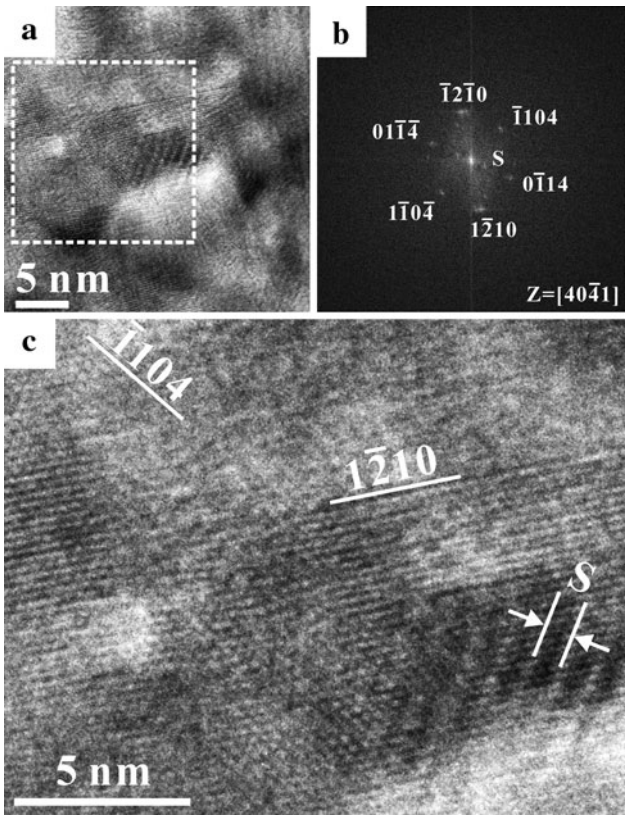

Fig. 7 **a** Lattice image, **b** and **c** 2-D forward and inverse Fourier transform, respectively, of the *square* region in (**a**) showing well-developed ($1\bar{2}10$) and $\{1\bar{1}04\}$ surfaces of the calcite nanocrystals. Note 1-D commensurate superstructure diffraction (denoted as *S*) with 3 times ($0\bar{1}14$) d-spacing in (**c**). The scale sample was taken from the steel pipe subjected to MWT under 100 G at pipe center, 0.1 s/cycle, and with an electric ground to the Earth

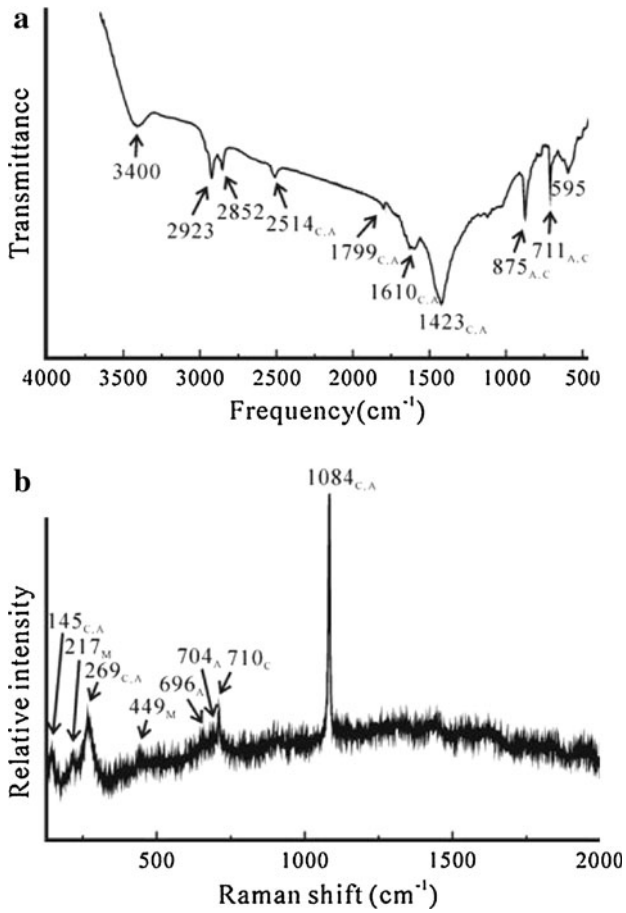

Fig. 8 **a** FTIR of OH-signified calcite (*C*), aragonite (*A*), and magnetite (*M*) of the same specimens as in Fig. 1, showing the OH^- stretch at 3,400 cm^{-1} and characteristic absorption bands of the three phases as labeled and assigned in text. The corresponding Raman spectrum **b** shows the characteristic peaks with assigned vibration modes in text. There is considerable frequency change due to defects and partial disorder (cf. text)

[23]. It is an open question whether tramp Fe ions, as clusters in the solution or on the surface of iron oxide crystals, have catalyzed the calcite nucleation.

The calcite nanoparticles, once nucleated, tended to assemble as rectangular colony with $\{11\bar{2}0\}$ and $\{10\bar{1}4\}$ preferred orientation, which can be attributed to $\{11\bar{2}0\}$- and $\{10\bar{1}4\}$-specific coalescence of the nanoparticles. The formation of $\{11\bar{2}0\}$ and $\{10\bar{1}4\}$ surfaces of calcite was apparently affected by the MWT. In fact, the cation–anion mixed $\{11\bar{2}0\}$ surface of calcite (see schematic drawing in Fig. 9a) is a stepped (S) face with one periodic bond chain (PBC) [24], which can be formed by the incorporation of trace elements into steps/kinks [25]. Whereas the cation–anion mixed $\{10\bar{1}4\}$ (see schematic drawing in Fig. 9b), the most stable principal surface of a face-centered rhombohedron pseudocell [26, 27] belongs to F face with two PBCs and hence a relatively low growth rate along its plane normal. It is likely that the combined effects of Lorentz force, precondensation of clusters and extra ions (such as Na^+ and Cl^-) in the solution caused $\{\bar{1}120\}$ and $\{\bar{1}014\}$ surface stabilization for the calcite nanocrystallites.

The attachment of calcium carbonate particulates on their flat surfaces to minimize surface energy is analogous to the assembly behavior of inorganic crystallites over a flat substrate, including that via so-called artificial epitaxy [28], or in solution [29–31]. (In colloidal hydrothermal solutions, anatase (TiO_2) has been shown to generate dislocations by imperfectly oriented attachment on a specific atomic plane [29], forming twin boundaries [30], or chain-like arrays [31] via oriented attachment on such planes.) Apparently, the calcite nanocrystals with cation–anion mixed $\{11\bar{2}0\}$ and $\{10\bar{1}4\}$ surfaces by the present MWT process were able to coalesce. Hydrolysis or hydrogen-bonding interaction on $\{11\bar{2}0\}$ and $\{10\bar{1}4\}$ surfaces could help align calcite nanoparticles in view of the mutual interaction of water and calcite [32]. However, it is not clear whether water ordering near the reconstructed calcite surfaces, as indicated by the molecular dynamics simulation results of calcite $\{10\bar{1}4\}$ surface in contact with water [33] and

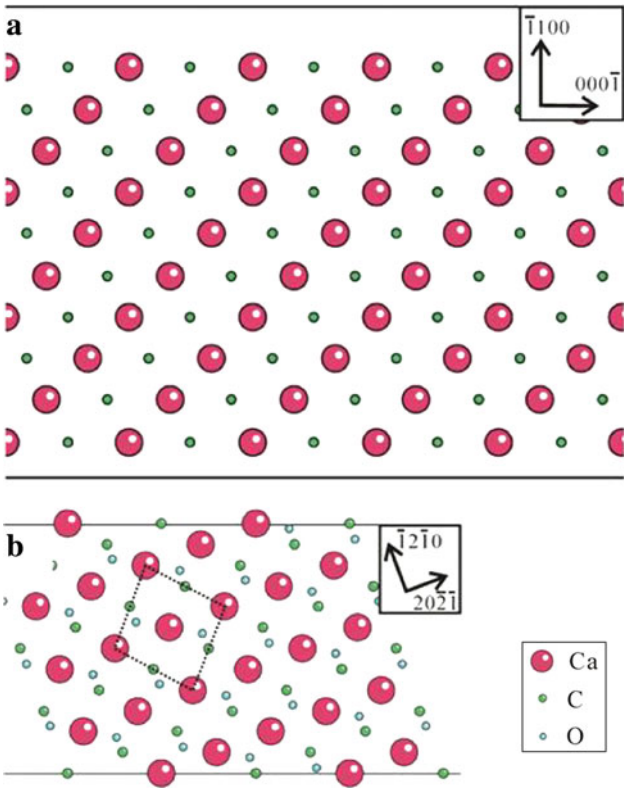

Fig. 9 Schematic drawings of (**a**) {11$\bar{2}$0} and (**b**) {10$\bar{1}$4} surfaces in unrelaxed state for calcite having Ca (*red*), O (*blue*), and C (*green*) atoms with decreasing size. Note Ca and C (representing CO_3^{2-}) atoms with point charges account for the cation–anion mixed surfaces in both (**a**) and (**b**), and a face-centered rhombohedron pseudocell including oxygen atoms is outlined by *dotted lines* in (**b**)

aqueous electrolyte solutions containing different concentrations of dissolved NaCl [34], could affect the coalescence of the present calcite nanoparticles.

Stability and Growth Habit of Aragonite

Specific physio-chemical and biological conditions of aqueous solution may cause metastable formation of the high-pressure phase of calcium carbonate, i.e. aragonite, at ambient pressure [35]. In this regard, sodium chloride tends to inhibit aragonite but favor calcite formation from a bicarbonate solution [36]. On the other hand, the presence of Mg^{2+} ions, e.g. in ancient sea water [37], in the internal shells of mollusks cultivated in artificial sea water [38] and over organic polymer matrices [39], was reported to favor the formation of aragonite. Furthermore, at one atmospheric pressure, the maximum probable temperature for the vaterite–calcite equilibrium boundary and the vaterite–aragonite metastable equilibrium boundary (both with a negative Clauseus–Clayperon dT/dP slope) was estimated to be 10 and 15°C, respectively [40]. This information enables the probable low-temperature phase relationships for the $CaCO_3$ system to be constructed [40], showing that the relative stability of the three polymorphs below 300 K is sensitive to pressure and temperature changes. It cannot be excluded that the dynamic magnetohydrodynamic force in the present MWT caused internal stress and lattice/polyhedral distortion of the $CaCO_3$ particles, as manifested by vibration spectroscopy and hence affect the packing scheme of Ca^{2+} and phase selection at room temperatures (Each oxygen atom is linked to two calcium atoms in fcc-like calcite and to three calcium atoms in hcp-like aragonite [41]).

In the present scale, the aragonite predominantly formed lath with unusual (0$\bar{1}$1) habit plane extending along [100] direction. This can be attributed to the anisotropic growth under the combined effects of PBC and precondensation in a dynamic process, as suggested for other molecular/ionic crystals with orthorhombic crystal structure such as $BaSO_4$ and $KC1O_4$ [42]. The (0$\bar{1}$1) habit plane of aragonite, a cation–anion mixed plane given the space group *Pcmn* [41], could be derived from face-centered planes of parent vaterite and/or calcite i.e. the F face with at least two PBCs [24] (Fig. 10). The [100] direction of aragonite has the shortest bonding distance between the nearest Ca^{2+} and CO_3^{2-} neighbor assuming with point charges [41], and hence a favorable growth direction with the most strong PBC for the preferred accommodation of the ions and/or ion clusters from solution.

It is worthwhile to note that the 3x commensurate superstructure parallel to the (0$\bar{1}$1) plane of aragonite can be attributed to stress-induced periodic shift of Ca ions and or CO_3 groups analogous to post-aragonite phase transitions in the alkaline-earth carbonates to form 2x2x1 superstructure [43]. Ordering of tramp ion impurities and Ca^{2+} in the aragonite lattice for such a commensurate superstructure is considered to be less likely via the present dynamic MWT process. The same argument can be extended to the 3x commensurate superstructure parallel to the (0$\bar{1}$14) plane of calcite.

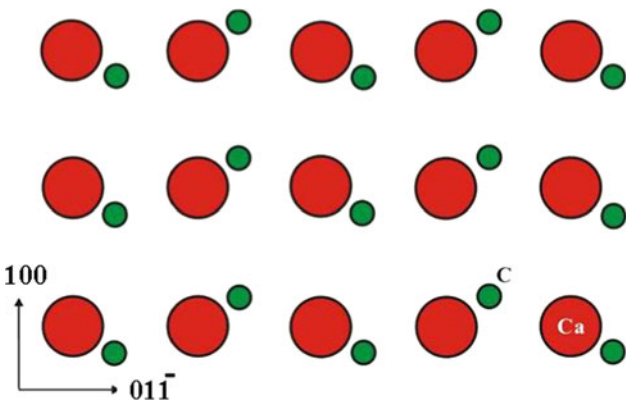

Fig. 10 Schematic drawings of the unrelaxed (0$\bar{1}$1) surface of aragonite, assuming Ca (*red*) and C (*green*, representing CO_3^{2-}) atoms have point charges for the cation–anion mixed surfaces

Nucleation and Growth of Submicron-Sized and (011)-Faced Magnetite

The present magnetite occurred as submicron-sized particles with well-developed (011) face besides the {111} and {100} facets regardless of MWT. This indicates that the magnetite was crystallized via an oxolation process of the ferrous and ferric irons in the oversaturated aqueous fluid regardless of an applied magnetohydrodynamic force. Internal oxidation of low-carbon steel would otherwise cause epitaxial intergrowth of iron oxides with the α-Fe substrate. In this connection, it is of interest to note that the oxidation scale consists of the epitaxial oxides of $RO + R_3O_4 + R_2O_3$ or $RO + R_3O_4$ (where R represents metal cations) coexisting with a metal alloy substrate such as aluminized coatings on Ni-based superalloys [44]. The oxidation alteration rim of the natural podiform chromitite deposit, i.e. so-called ferritchromit, also contains the epitaxial oxides of $RO + R_3O_4 + R_2O_3$ or $RO + R_3O_4$ [45].

The precondensation of clusters and extra ions (such as Na^+ and Cl^- as mentioned) in the solution and additional effect of Lorentz force may help stabilize the cation–anion mixed (011) faces with a single edge-shared octahedra chain, besides another cation–anion mixed surface (100) with two such chains. The {111} face being cation–anion unmixed and without such chain, yet with close-packed oxygen atoms, is less stable for the present magnetite. (The {001}, {110}, and {111} have 2, 1 and 0 PBCs, respectively, in terms of the edge-shared octahedral [46] for the case of the spinel-type isostructure.)

Implications

The present experimental results indicate that the ferrous and ferric irons with spin magnetic moment in the aqueous solution were incorporated as euhedral magnetite particles and hardly dissolved in calcite and aragonite consisting of ions with zero-spin magnetic moment. Besides, specific surfaces with mixed cations and anions, rather than spherical particles as assumed for the theoretical calculation [14], facilitated the growth and coagulation of both magnetic and nonmagnetic crystals via the present MWT process. The nucleation and growth mechanism via the present MWT can therefore be summarized ("Appendix 2") as: (1) enhanced adsorption of mixed cations and anions on the faceted nuclei rotating under an applied magnetic field and fluid flow; (2) (hkl)-specific coalescence and ledge growth of the crystallites; (3) anchorage and sedimentation of the crystallites with planar defects on the pipe by the magnetohydrodynamic force.

In general, the competitive deposition of soft/hard calcium carbonate and iron oxides on an industrial steel pipe subjected to MWT would also depend on oxolation kinetics under magnetohydrodynamic force, rotation/translation kinetics of nanoparticles under Lorentz force, and sedimentation versus dissolution/spalling rates under the influence of temperature, concentration, flow rate, and the applied magnetic field. In any case, MWT would cause a beneficial larger particle size for the scale deposit to be more removable from the steel substrate.

The driving force in terms of supercooling and oversaturation of ions under the influence of H_2O and magnetohydrodynamic forces was likely not large in the present dynamic growth of calcite, aragonite, and magnetite with well-developed planar faces, as the particle morphology would otherwise be dendritic/spherulitic in view of metal solvent and H_2O-facilitated dendritic growth of atom close-packed crystals such as diamond [47]. In fact, aqueous solution containing tar and additional ions, such as SO_4^{2-}, Si^{4+}, Mg^{2+} Al^{3+} under high pH condition in our additional MWT experiment up to 3 months, did cause the formation of spherulitic particulates.

Finally, it is of interest to know whether surface-specific assembly and planar defects of nanocrystals by MWT, as presented here, can be extended to calcium carbonate minerals with hierarchical structures and various morphologies when tailored by temperature and polymer concentration [48]. The effect of magnetic field strength on the shape and defect microstructure development of magnetic materials, such as 1-D Ni nanowires via a hydrazine reduction route in aqueous ethanol solutions at external magnetic field up to 0.5 T [49], is also worthwhile to explore in the future. (According to ref. [49], under a low magnetic field of 0.05 T, short, thick, and flexural Ni wires occurred. When the strength of the magnetic field was increased to 0.2 T, nanowires having aspect ratio of about 1,000 with average diameter of 200 nm and length of 200 μm were formed. However, there was little change observed on morphology of nanowires when magnetic fields increased from 0.2 T to 0.5 T.)

Conclusions

1. The calcite and aragonite particles deposited on the steel substrate by a dynamic MWT process have characteristic cation–anion mixed surfaces and planar defects besides the common OH^- signature and lattice/polyhedra distortion.
2. Calcite formed faceted nanoparticles having 3x $(0\bar{1}14)$ commensurate superstructure and with well-developed $\{11\bar{2}0\}$ and $\{10\bar{1}4\}$ surfaces to show preferred orientations.
3. Aragonite were lath-like having 3x $(0\bar{1}1)$ commensurate superstructure and with well-developed $(0\bar{1}1)$ surface extending along [100] direction up to micrometers in length.

4. The (hkil)-specific coalescence of calcite and rapid lath growth of aragonite under the combined Lorentz force and precondensation effects caused a beneficial larger particulate/colony size of the $CaCO_3$ to be removed from the steel substrate.
5. The magnetite particles coexisting with calcite and aragonite in the scale are submicron in size and have well-developed {011} surfaces regardless of MWT.

Acknowledgments Supported by China Steel Corporation under contract 98T6D0013E. We thank Drs. M. F. Lai and D. Gan for helpful discussions on magnetohydrodynamic forces, an anonymous referee for constructive comments, and the Center for Nanoscience and Nanotechnology at NSYSU for FTIR and Raman analyses.

Appendix 1

Experimental setup for the MWT conducted in this study.

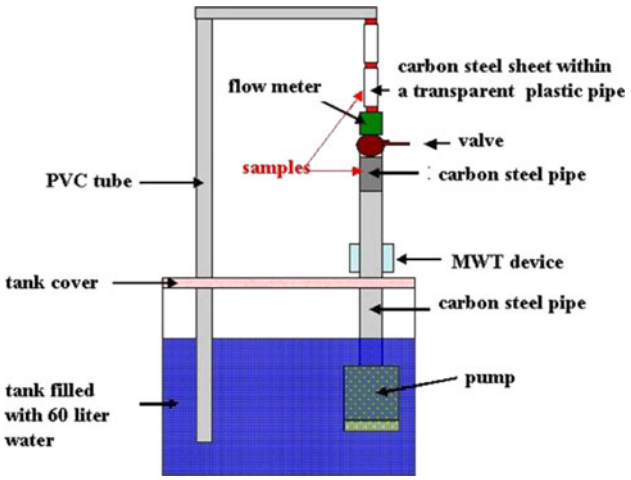

Appendix 2

Schematic drawing of the crystal nucleation and growth mechanism via MWT: (1), enhanced adsorption of mixed cations and anions on the faceted nuclei rotating under an applied magnetic field and fluid flow rate, (2), (hkl)-specific coalescence and ledge growth of the crystallites, (3), anchorage and sedimentation of the crystallites with planar defects on the pipe by magnetohydrodynamic force.

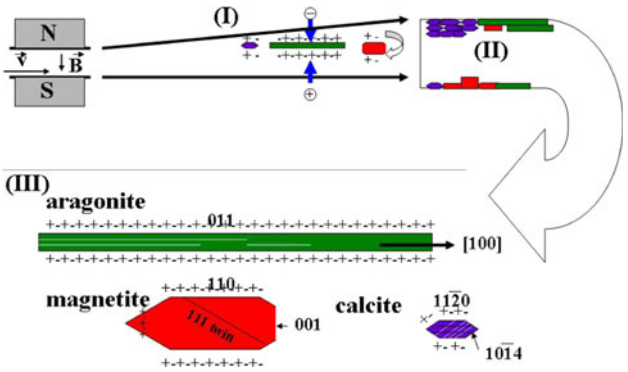

References

1. T. Vermeiren, Corrosion Technol. **5**, 215 (1958)
2. R.E. Herzog, Q. Shi, J.N. Patil, J.L. Katz, Langmuir **5**, 861 (1989)
3. K. Higashitani, K. Okamura, S. Hatade, J. Colloid Int. Sci. **152**, 125 (1992)
4. K. Higashitani, A. Kage, S. Katamura, S. Hatade, J. Colloid Int. Sci. **156**, 90 (1993)
5. I. Dobrevski, M. Boneva, B. Bonev, Russ. J. Apply. Chem. **66**, 422 (1993)
6. E. Dalas, P.G. Koutsoukos, J. Cryst. Growth **96**, 802 (1993)
7. P.P. Coetzee, M. Yacoby, S. Howell, Water SA **22**, 319 (1996)
8. P.P. Coetzee, M. Yacoby, S. Howell, S. Mubenga, Water SA **24**, 77 (1998)
9. J. Svoboda, Int. J. Miner. Process **8**, 377 (1981)
10. J. Svoboda, J. Colloid Interface Sci. **94**, 37 (1983)
11. K.W. Busch, M.A. Busch, Desalination **109**, 131 (1997)
12. O.T. Krylov, I.K. Vikulova, V.V. Eletskii, N.A. Rozno, V.I. Klassen, *Influence of Magnetic Treatment on the Electrokinetic Potential of a Suspension of $CaCO_3$.* (Plenum, New York, 1986). UDC541.182.65:537.6
13. O.T. Krylov, N.A. Rozno, E.I. Funberg, V.I. Klassen, Elektron. Obrabotka Mater. **2**, 53 (1987)
14. L.C. Lipus, J. Krope, L. Crepinsek, J. Colloid Interface Sci. **236**, 60 (2001)
15. J.M.D. Coey, S. Cass, J. Magn. Magn. Mater. **209**, 71 (2000)
16. S. Kobe, G. Dražić, P.J. McGuiness, J. Stražišar, J. Magn. Magn. Mater. **236**, 71 (2001)
17. C.Z. Liu, MS Thesis, National Sun Yat-sen University, Taiwan, 2010
18. H.H. Adler, P.F. Kerr, Am. Mineral. **47**, 700 (1962)
19. H.C. Liese, Am. Mineral. **52**, 1198 (1967)
20. J. Urmos, S.K. Sharma, F.T. Mackenzie, Am. Mineral. **76**, 641 (1991)
21. O.N. Shebanova, P. Lazor, J. Solid State Chem. **174**, 424 (2003)
22. E.M. Pouget, P.H.H. Bomans, J.A.C.M. Goos, P.M. Frederik, G. de With, N.A.J.M. Sommerdijk, Science **323**, 1455 (2009)
23. Y. Takita, M. Eto, H. Sugihara, K. Nagaoka, Mater. Lett. **61**, 3083 (2007)
24. P. Hartman, W.G. Perdock, Acta Crystall. **8**, 49 (1955)
25. J. Paquette, R.J. Reeder, Geochim. et Cosmochim. Acta **59**, 735 (1995)
26. S. Hwang, M. Blanco, W.A. Goddard, J. Phys. Chem. B **105**, 10746 (2001)
27. A. Putnis, *Introduction to Mineral Sciences.* (Cambridge University Press, London, 1992), p. 35 and p. 388–390
28. E.I. Givargizov, *Oriented Crystallization on Amorphous Substrates.* (Plenum, New York, 1991)

29. R.L. Penn, J.F. Banfield, Science **281**, 969 (1998)
30. R.L. Penn, J.F. Banfield, Am. Mineral. **83**, 1077 (1998)
31. R.L. Penn, J.F. Banfield, Geochimica et Cosmochim. Acta **63**, 1549 (1999)
32. P. Geissbuhler, P. Fenter, E. DiMasi, G. Srajer, L.B. Sorensen, C.N. Sturchio, Surf. Sci. **573**, 191 (2004)
33. T.D. Perry IV, R.T. Cygan, R. Mitchell, Geochim. et Cosmochim. Acta **71**, 5876 (2007)
34. D. Spagnoli, S. Kerisit, S.C. Parker, J. Crystal Growth **294**, 103 (2006)
35. N. Wada, K. Yamashita, T. Umegaki, J. Colloid Interface Sci. **212**, 357 (1999) and literature cited herein
36. Y. Kitano, Bull. Chem. Soc. Jpn. **35**, 1973 (1962)
37. S.M. Porter, Science **316**, 1302 (2007)
38. A.G. Checa, C. Jiménez-López, A. Rodríguez-Navarro, J.P. Machado, Marine Biol. **150**, 819 (2007)
39. A. Sugawara, T. Kato, Chem. Comm. **6**, 487 (2000)
40. J.N. Albright, Am. Mineral. **56**, 620 (1971)
41. W.L. Bragg, G.F. Claringbull, *The Crystalline State–Vol. IV Crystal Structures of Minerals* (Cornell University Press, Ithaca, 1965), pp. 129–134
42. P. Hartman, W.G. Perdock, Acta Crystall. **8**, 525 (1955) and literature cited therein
43. C.C. Lin, L.G. Liu, J. Phys. Chem. Solids **58**, 977 (1997)
44. M.J. Tsai, P. Shen, Mater. Sci. Eng. **83**, 135 (1986)
45. P. Shen, S.L. Hwang, H.T. Chu, R.C. Jeng, Am. Mineral. **73**, 383 (1998)
46. C.H. Lin, C.N. Huang, S.Y. Chen, Y. Zheng, P. Shen, J. Phys. Chem. C **113**, 19112 (2009)
47. I. Sunagawa, J. Crystal Growth **99**, 1156 (1990)
48. X.H. Gao, A.W. Xu, S.H. Yu, Cryst. Growth Des. **8**, 1233 (2008)
49. L.Y. Zhang, J. Wang, L.M. Wei, P. Liu, H. Wei, Y.F. Zhang, Nano-Micro. Lett. **1**, 49 (2009)